Additive Manufacturing 117 (2026) 105076

Contents lists available at ScienceDirect

Additive Manufacturing

journal homepage: www.elsevier.com/locate/addma

Research paper

In situ mechanical foaming in fused filament fabrication

Lars Eisele *, Anselm Heuer, Wilfried V. Liebig

Karlsruhe Institute of Technology, Institute for Applied Materials – Materials Science and Engineering (IAM-WK), Engelbert-Arnold-Straße 4, 76131 Karlsruhe, Germany

ARTICLE INFO

Keywords:
Additive manufacturing (AM)
Porous media
Gas injection
Microcellular foam
Bubble generation

ABSTRACT

In the context of lightweight design and functional integration, the generation of foamed structures in additive manufacturing represents a key technological objective. Conventional foaming methods often rely on chemical blowing agents or physical foaming in downstream processes such as autoclaves, which require complex process chains and high energy input. To address these limitations, this work presents a first feasibility demonstration of a process-integrated mechanical foaming approach for material extrusion, ensuring continuous production in an in-line foaming process. A modular nozzle was developed, in which carbon dioxide is injected into the polymer melt under high pressure during extrusion. Gas enters the melt through a porous medium embedded in the nozzle, enabling controlled gas transfer while preventing melt backflow. This mechanism facilitates mechanical foaming within the nozzle itself, eliminating the need for separate process stages. Systematic material screening showed that metallic porous media with submicron pore diameters provide sufficient resistance to melt intrusion while allowing stable gas injection. Extrusion trials with polylactic acid confirmed that the resulting foam morphology depends on the gas-to-melt mass flow ratio, yielding uniform microcellular structures with porosities up to 25 % and mean pore diameters around 100 µm. The presented results demonstrate that stable foam extrusion based on mechanical foaming through in-nozzle gas injection is feasible, and they establish the foundation for further investigations aimed at process refinement towards finer microcellular structures and fully additively manufactured foamed components.

1. Introduction and motivation

The combination of additive manufacturing (AM) and lightweight design offers high potential for functional integration and the manufacturing of resource-efficient components. In material extrusion (MEX) based AM processes, in addition to reducing the infill, a variety of techniques are already used to create foam structures through the use of physical or chemical blowing agents. These methods all rely on the fundamental mechanism of gas expansion within a polymer matrix. According to Nofar et al., foaming approaches can be broadly categorized into *in situ* and *ex situ* processes, depending on whether foam formation occurs during the AM process or in a downstream post-processing step [1]. A further distinction is made between physical and chemical foaming. Physical foaming involves dissolving compressed gas into the polymer and subsequently releasing it by pressure reduction, while chemical foaming relies on the thermal decomposition or chemical reaction of solid blowing agents incorporated into the melt [2–4].

A key parameter used to characterize the resulting foam structure is the expansion ratio Φ_A, which quantifies the relative increase of the pore-free polymer volume V_K by the gas volume V_G introduced during foaming [5]:

$$\Phi_A = \frac{V_G}{V_K} = \frac{\Phi_s}{1-\Phi_s}, \tag{1}$$

where the porosity Φ_s is defined as the ratio of gas volume to total volume:

$$\Phi_s = \frac{V_G}{V_{Total}}. \tag{2}$$

In *ex situ* foaming, the part is first additively manufactured and subsequently saturated with gas in a high-pressure autoclave. After gas dissolution, a slow pressure drop induces a metastable polymer-gas mixture, which foams upon heating. Although foaming degrees of up to 40 % have been reported using this method, the need for an additional autoclave step and extended saturation times limits its practicality [6, 7].

In contrast, *in situ* foaming integrates the blowing agent into the polymer before or during AM. One approach involves pre-saturating the filament with gas in an autoclave, similar in principle to post-foaming, but applied prior to material extrusion. However, this method

* Corresponding author.
E-mail address: lars.eisele@kit.edu (L. Eisele).

https://doi.org/10.1016/j.addma.2026.105076
Received 26 September 2025; Received in revised form 21 November 2025; Accepted 2 January 2026
Available online 9 January 2026

is sensitive to gas loss: Li et al. observed a significant reduction of CO_2 content within just 10 h of storage [8], and Zhang et al. showed a drop in expansion ratio from 65 % to 35 % after 120 h [9]. Moreover, complex pressure and temperature profiles are required to prevent premature foaming [10].

In chemical in situ foaming, blowing agents must be incorporated during compounding. Here, careful temperature control is critical to avoid uncontrolled gas release during mixing [5]. Reported expansion ratios vary widely, with values up to 145 % for optimized systems [11], but also as low as 23 % to 25 % when premature reactions occur [12]. Thermally expandable microspheres (TEMs) represent a promising physical in situ approach [7,13–15]. Like chemical blowing agents, TEMs are incorporated via compounding, but foam generation occurs by thermal expansion of a volatile liquid encapsulated within a polymer shell [5]. As no gas dissolution is required, foam formation is more controllable, provided that the processing temperature during compounding remains below the expansion threshold. When homogeneously dispersed, TEMs can produce highly uniform cellular structures with expansion ratios between 85 % and 250 %, depending on filler content [16].

While early studies offered only limited control over the resulting foam density and morphology in foamed AM parts, recent work has demonstrated that microcellular structures in extrusion-based AM can be regulated more precisely. Zhou et al. showed that, for TEM-based filaments, macroscopic foam density and bead geometry can be stabilized through spatiotemporal monitoring of the thermal field, strand geometry and material feed, combined with data-driven local parameter adjustments that suppress secondary expansion and reduce surface roughness [17]. Esposito et al., in turn, demonstrated that CO_2-pre-saturated PLA filaments can produce orientation-graded microfoams when well-defined thermal gradients are imposed in the hot end, yielding the characteristic double morphology with axially and radially oriented cells [18]. These developments illustrate that improved structural control is achievable in AM foaming. Nevertheless, despite the diversity of strategies explored, most current AM-compatible foaming methods face significant limitations. These include the need for additional equipment (e.g., autoclaves or dedicated compounding steps for incorporating chemical blowing agents or TEMs), narrow processing windows to prevent premature foaming, and time-dependent gas loss, especially for pre-saturated filaments. Tammaro et al. address these limitations by integrating physical foaming into the printing process without requiring upstream saturation steps [19]. In their solvent-assisted approach, PLA filament is guided through an acetone bath prior to extrusion, where the polymer swells and its free volume increases, enabling the uptake of volatile species. During melting and the subsequent pressure drop at the nozzle exit, the absorbed solvent desorbs and nucleates microcells. By adjusting the absorption and desorption times, different overall foaming levels and cell densities can be obtained, demonstrating that solvent-induced gas uptake provides a further route to influencing microcellular structure directly during AM. While this method enables in-process foaming without additional steps, it is inherently governed by solvent diffusion and thermal desorption kinetics, which limit sharp on–off transitions and make it difficult to produce fully solid and foamed regions within the same build. Motivated by these constraints, the present work introduces an in-nozzle gas-injection concept based on a porous metallic insert, which acts as a barrier against melt backflow while enabling controlled CO_2 transfer into the polymer melt. Rather than relying on gas dissolution followed by nucleation, as in conventional physical foaming, or on thermally activated expansion of pre-compounded agents, the proposed approach follows a mechanical foaming principle, in which fine gas bubbles are introduced directly into the melt through the pores of the insert. This architecture provides a modular and retrofittable route for process-integrated foaming and offers the potential for sharp porosity transitions and for the fabrication of locally unfoamed layers by adjusting the gas inflow. To assess the feasibility of this concept, porous materials of different pore sizes are systematically examined with respect to their ability to resist polymer infiltration. Their suitability is evaluated through dedicated infiltration experiments using a custom-built test rig that quantifies penetration behaviour under defined process pressures. The most promising material is subsequently implemented in the nozzle and investigated in continuous foaming trials, in which individual strands are extruded directly into the ambient environment to analyse process stability and the resulting morphology. Finally, the influence of the key parameters – gas pressure, nozzle temperature and feed rate – on the resulting foam structure is investigated and qualitatively related to the ratio of gas to polymer mass flow. Foam characterisation is performed using gravimetric density measurements (Archimedes' principle), micro-computed tomography, and optical as well as scanning electron microscopy. Building on these findings, future work incorporating additional in-process measurement techniques will aim to establish a quantitative relationship between these parameters and the resulting cellular morphology, enabling finer structural control and the fabrication of fully foamed components.

2. Materials and methods

2.1. Materials

This study involves two distinct material classes: thermoplastic polymers processed by extrusion, and porous materials (PM) used as functional elements for gas injection in the nozzle assembly.

Thermoplastic polymers

Polylactic Acid

All extrusion experiments were conducted using the thermoplastic polymer polylactic acid (PLA), type Renkforce RF-4511188. The material was supplied as a black filament with a diameter of 1.75 mm. The data sheet does not specify a density value. Archimedes measurements performed in this work yielded a density of $1.25\,g\,cm^{-3}$, which is approximately 0.8 % higher than the consistently reported literature value of around $1.24\,g\,cm^{-3}$ [20–23]. The recommended processing temperature according to the data sheet lies between 190 °C and 230 °C.

Acrylonitrile Butadiene Styrene

The thermoplastic acrylonitrile butadiene styrene (ABS) used for infiltration experiments was a general-purpose grade, Terluran GP35, supplied by INEOS Styrolution Group GmbH. Its density is reported as $1.04\,g\,cm^{-3}$ [24], which was confirmed through Archimedean measurements on individual granules. The recommended processing temperature lies in the range of 220 °C to 260 °C.

Porous materials for gas injection

To enable gas injection into the nozzle while simultaneously preventing polymer melt infiltration, porous materials (PM) were employed as functional elements within the nozzle. Several candidate PMs were systematically investigated to identify a suitable material. Throughout this work, porous materials are designated as PM-[Material]-[Porosity in %]-[Mean pore diameter in μ m], e.g., PM-Silica-50-1 refers to a silica-based ceramic with 50% porosity and a mean pore diameter of 1 μm.

Porous Ceramics

The silica-based ceramic Rapor P1 was supplied by Rauschert GmbH and processed in the form of hollow cylinders with an outer diameter (OD) of 4.2 mm, an inner diameter (ID) of 2.5 mm, and a length (L) of 15 mm. According to the manufacturer, the material features an open porosity in the range of 50 % to 52 %, a mean pore diameter of 1 μm, a density of $1.0\,g\,cm^{-3}$, and a thermal stability of up to 600 °C. This material is referred to PM-Silica-50-1.

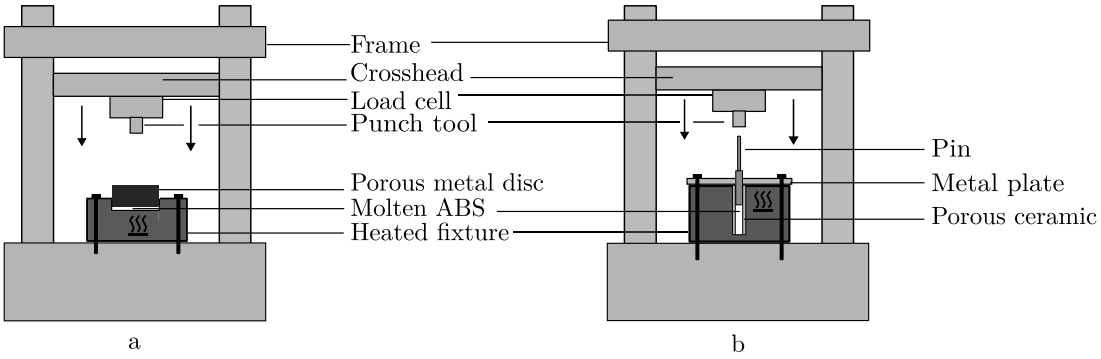

Fig. 1. Schematic setups for infiltration tests for (a) Metallic PMs and for (b) Ceramic PMs.

Porous Metals

Several sintered metal discs were used in this study. One specimen made of stainless steel 316L was provided by Hengko Technology Co., Ltd. and featured a diameter of 20 mm, a height of 5 mm, a mean pore diameter of 0.1 µm, and an open porosity of 17 %. This material is designated as PM-316L-17-0.1. Further stainless steel samples were obtained from AMES Group Sintering, S.A. The variant PM-316L-36-12 had a mean pore diameter of 12 µm and a porosity of 36 %, while the variant PM-316L-37-25 exhibited a mean pore diameter of 25 µm and a porosity of 37 %. Additionally, sintered bronze discs of type B85 from AMES Group Sintering S.A., composed of 89 % copper and 11 % tin, were used. These specimens had a diameter of 16 mm, a height of 10 mm, an open porosity of 40 %, and a mean pore diameter of 82 µm. This material is referred to as PM-Bronze89/11-40-82.

2.2. Polymer infiltration testing

To preselect a suitable PM for integration into the nozzle system, preliminary infiltration experiments were conducted to assess the resistance of different PM types against polymer infiltration. These tests served to identify candidates capable of allowing gas permeation while withstanding direct contact with the polymer melt. The experiments were carried out by using a zwickiLine Z2.5 TN testing machine from ZwickRoell GmbH & Co. KG, equipped with a 2.5 kN load cell. Each PM was weighed five times prior to testing by using an ME204T/00 analytical balance from Mettler-Toledo GmbH, then pressed into molten ABS and reweighed after cleaning to determine the mass gain owing to polymer infiltration.

An electrically heated aluminum fixture was developed to melt the polymer, with temperature control implemented via cartridge heaters, thermocouples, and a PID controller. The fixture featured a cylindrical cavity to hold ABS pellets (approximately 0.7 g) and was mounted on the machine base. To minimize leakage between the outer surface of the PM specimens and the fixture walls, the contact interface was sealed using PTFE thread seal tape prior to insertion. Two fixture variants were used to account for differing sample geometries. These are shown in Fig. 1. Force application was performed using a cylindrical punch (12 mm diameter, 30 mm length), which transmitted the load from the machine to the sample. The pressing procedure followed comprising initial contact with a force of 50 N, a ramp-up phase to the target force at 20 N s^{-1}, and a hold time of 300 s. After pressing, all specimens were cleaned with acetone-soaked cloths to remove surface residues and PTFE tape, then dried using compressed air and weighed again. If the relative mass gain was less than 0.01 %, the specimen was reused with a higher target force; otherwise, a new sample was used. For the stainless steel discs with 20 mm diameter, ten force levels between 200 N and 2000 N were applied in increments of 200 N. This corresponds to a maximum pressure of 63 bar, which reflects the maximum extrusion pressure previously determined for the system in a separate preliminary test. For samples with differing cross-sectional areas, the applied force was adjusted according to the relation $F = p \cdot A$ to maintain consistent pressure levels across all materials.

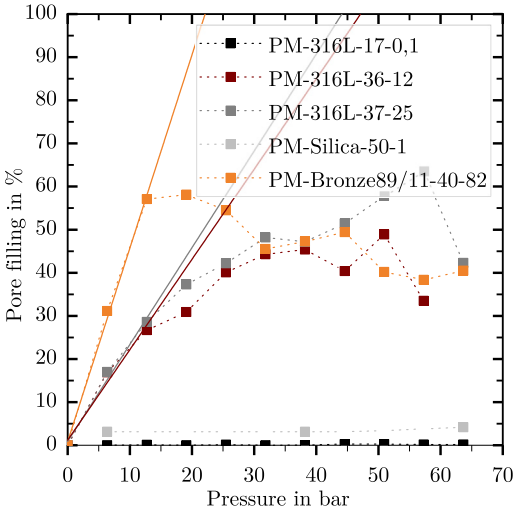

Fig. 2. Percentage of pore volume filled with polymer melt as a function of applied pressure for various PM. Solid lines indicate the expected trend under ideal, leakage-free conditions, extrapolated from the initial slope.

Fig. 2 shows the percentage of pore volume filled with polymer as a function of applied pressure. The values were determined gravimetrically by relating the measured mass gain to the theoretical maximum pore volume, calculated based on the known porosity ϕ_{PM}, specimen volume V_{PM}, and ABS density ρ_{ABS} by using Eq. (3):

$$\text{Pore filling (\%)} = \left(\frac{\Delta m_{\text{measured}}}{V_{PM} \cdot \frac{\phi_{PM}}{100} \cdot \rho_{ABS}} \right) \cdot 100. \tag{3}$$

As shown in the figure, most PM exhibit an initially increasing pore filling with pressure. However, at higher pressures, the curves deviate from linearity. This non-monotonic behaviour is attributed to leakage at the PM-fixture interface, which occurs despite PTFE sealing and causes the PM to be increasingly pressed against the fixture rather than remaining in contact with the melt. Assuming stationary flow conditions, the infiltration behaviour can be described by using Darcy's law

$$Q = \frac{A}{e} \cdot \frac{k}{\eta} \cdot \Delta p, \tag{4}$$

where Q is the volumetric flow rate, A the infiltrated area, e the specimen thickness, k the permeability – an empirical constant that correlates with the mean pore diameter of the PM – η the melt viscosity, and Δp the pressure differential [25,26]. For constant values of A, e,

k, and η, the volumetric flow rate is therefore directly proportional to the applied pressure. Since the contact time between PM and melt was fixed for all experiments, the infiltrated volume – and hence the measured pore filling – should also increase linearly with pressure under ideal, leakage-free conditions. The solid lines in Fig. 2 represent this expected trend, extrapolated from the initial slope of each curve. Results confirm that pore infiltration decreases with lower porosity and smaller average pore size. For PM-316L-17-0.1 and PM-Silica-50-1, the pore filling remains negligible. However, owing to its high brittleness and frequent mechanical failure during testing, the ceramic PM was deemed unsuitable for nozzle use.

A supplementary SEM cross-section of PM-316L-17-0.1 tested at the seventh pressure level (~ 45 bar) revealed a local pore filling of approximately 4 %. Using the known contact time during this pressure stage, the corresponding infiltration rate can be estimated and, via Darcy's law (see Eq. (4)), related to the applied melt pressure. This enables an extrapolation of the expected infiltration behaviour under operating conditions. During the extrusion trials, however, no infiltration is expected to occur because the external CO_2 pressure was always set higher than the opposing melt pressure, ensuring gas influx while preventing melt ingress into the porous medium. Based on these findings, PM-316L-17-0.1 was selected as the gas-permeable insert for the nozzle configuration described in Section 2.3. For future applications, however, that may involve switching between foamed and unfoamed deposition during manufacturing of complete parts, the gas pressure should be dynamically adjusted relative to the local melt pressure: it must remain sufficiently high to prevent melt infiltration into the porous medium, yet low enough to avoid gas ingress into the melt. This controlled pressure window is necessary because melt infiltration would irreversibly reduce the permeability of the porous medium over time [27].

2.3. Material extrusion and foaming setup

A modular extrusion system was developed, combining MEX with a high-pressure gas injection unit, as illustrated in Fig. 3. The motion system enables movement of the heated build platform along the x- and y-axes, while the extruder is positioned along the vertical z-axis using two lead screws. The system employs a direct-drive extruder equipped with a brass nozzle featuring an orifice diameter of 0.4 mm. The nozzle is heated by a cartridge heater with a power rating of 40 W and mounted into a Revo Six cold-end assembly from E3D. The maximum operating temperature of the nozzle is 280 °C. To enable gas injection, the nozzle was modified to incorporate a hydraulic hose with a length of 1 m and an inner diameter of 4 mm. Carbon dioxide (CO_2) was supplied from a pressurized gas cylinder. At room temperature, the cylinder contained liquefied gas with an overlying vapor phase and exhibited a saturation pressure of approximately 60 bar. Gas was withdrawn from the upright cylinder and the target process pressure was adjusted individually using a pressure regulator of type Vulkan F60/200.

To enable gas injection, a modular nozzle concept was implemented. As illustrated in Fig. 4, the original Revo nozzle was modified by replacing the outlet orifice with an external M6 male thread at its lower end. This modified component is referred to as the *base nozzle*. It was designed to accommodate a custom-developed modular nozzle, enabling gas to be injected from the high-pressure CO_2 supply into the polymer melt via a porous material. To ensure a gas-tight seal, four to five turns of PTFE thread seal tape were wrapped around the thread. All parts were assembled using a defined torque of 0.8 Nm to prevent thread damage. The modular nozzle, shown in Fig. 5, featured an internal M2.5 thread to mount a gas adapter and incorporated an inserted PM as hollow cylinder. This porous metal was wire-cut from the disc described in Section 2.1 and manufactured as a hollow cylinder (inner diameter: 2 mm, outer diameter: 4 mm, length: 15 mm). A guidance geometry ensured correct positioning and maintained the annular gas gap only in the upper region to enhance alignment and sealing surface area. The PM was axially compressed between two PTFE gaskets to prevent leakage of gas and polymer melt. Gas supplied via the adapter was able to spread radially within the gap and permeate through the porous material into the melt channel. The assembly of base nozzle and modular nozzle is referred to hereafter as the PM nozzle. Strands produced via gas injection extrusion were extruded freely into the ambient environment.

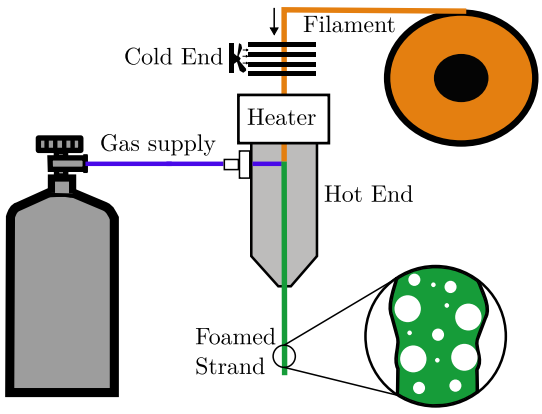

Fig. 3. Schematic of the extrusion system with integrated gas injection.

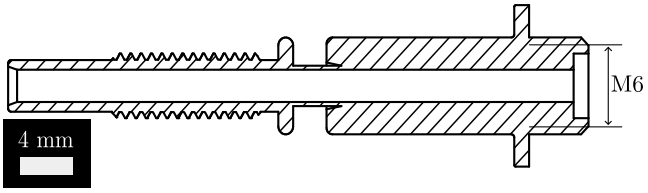

Fig. 4. Technical drawing of the modified Revo nozzle (base nozzle). The longitudinal section reveals the integrated M6 thread that enables modular attachment of the custom gas injection unit.

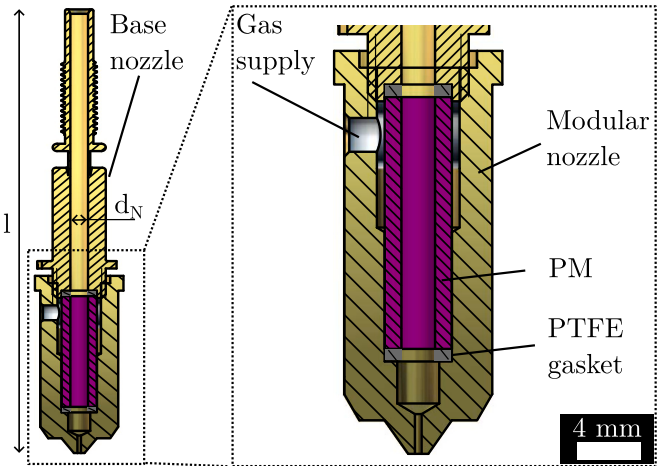

Fig. 5. PM-nozzle configuration with integrated guidance and dual PTFE gaskets. The hollow porous cylinder allows radial diffusion of gas into the polymer stream.

2.4. Parameter variation

After establishing the PM-nozzle as a configuration capable of stable foam extrusion, a parameter study was conducted to investigate the influence of key process variables. The investigated parameters

included nozzle temperature T_N, gas pressure p_G, and feed rate v. Other potentially relevant factors affecting the foaming behaviour, such as gas injection duration or pulsation, were not varied in this initial feasibility study in order to ensure stationary process conditions. Three temperature levels (200 °C, 230 °C and 260 °C) and three pressure levels (30 bar, 40 bar and 50 bar) were combined with three feed rates (0.5 mm s^{-1}, 2 mm s^{-1}, 3.5 mm s^{-1}), resulting in 27 unique parameter sets. The temperature window was selected such that the lowest level remains safely above the PLA melting temperature (approximately 170 °C [19]) even at high feed rates and correspondingly short residence times, while the upper limit avoids thermal degradation, which becomes significant only above approximately 280 °C [19,28]. The chosen feed rates span the typical range used in FFF processes and were selected to cover both low- and high-throughput conditions [29]. The lower gas-pressure limit was determined through preliminary tests, during which foaming ceased below approximately 30 bar at medium nozzle temperature and feed rate stage. The upper pressure limit was constrained by the available CO_2 cylinder pressure (approximately 60 bar) and by the practical requirement to avoid frequent cylinder replacement during experimentation. For each configuration, strands were continuously extruded into ambient air for a duration of two minutes with CO_2 as the introduced gas. Since changing temperature and pressure required heating/cooling phases or manual adjustments of the pressure regulator, the polymer melt remained stationary inside the PM-nozzle during these transitions while gas injection continued. To compensate for potential effects of residence time, a purge strand of 100 mm length was extruded prior to each new parameter set. In contrast, changes in feed rate were implemented immediately without a purge step. Preliminary tests revealed that the heating capacity of the cartridge heater was insufficient to maintain 260 °C throughout the entire nozzle assembly. Therefore, the nozzle was thermally insulated with a nonwoven for the duration of the parameter study.

The extruded strands were labelled using the format v[feed rate]-T[nozzle temperature]-p[gas pressure], e.g., v2-T260-p40 for a strand produced at 2 mm s^{-1}, 260 °C, and 40 bar.

2.5. Characterisation methods

2.5.1. Micro-computed tomography

Foam morphology and porosity were characterised, among other methods, using a micro-computed tomography (μCT) scanner of type YXLON Precision. Scanning was carried out with an acceleration voltage of 130 kV and a target current of 0.05 mA. A total of 3000 projections were acquired using a flat-panel detector (XRD1620 AN, Perkin Elmer) with a resolution of 2048 px × 2048 px. To reduce noise, an exposure time of 1000 ms was selected. Volume reconstruction was performed using the FDK algorithm implemented in VGStudio MAX 3.4 by Volume Graphics GmbH. The resulting isotropic voxel size of the reconstructed data was 7.8 μm. For tomography, strand specimens of approximately 20 mm in length were fixed vertically on a custom-designed sample holder using a two-component adhesive. Image processing and quantitative evaluation were performed in VGStudio MAX 2024.3. For each strand, a region of interest (ROI) was defined and reoriented using the *Simple Alignment* tool to align one axis with the strand axis. Based on this ROI, cross-sectional slices and 3D views were generated. Porosity analysis was conducted using the *VG EasyPore* algorithm, which identifies pores via localized grayscale thresholds. Prior to pore detection, a machine learning-based segmentation was performed with the *Paint & Segment* tool, trained on manually labelled air and polymer regions. This segmentation step was required to reconstruct a geometrically accurate material surface, which serves as the input for surface determination and pore extraction in *VG EasyPore*. The segmentation was prone to errors when macropores or numerous surface-connected pores were present, as the material boundaries could not be correctly delineated. Therefore, strand sections without such artifacts were deliberately selected. Surface determination and pore extraction were subsequently carried out within the segmented volume. The resulting parameters included total porosity, mean pore diameter and pore density. Pore density was calculated as the number of segmented pores divided by the analysed strand volume. For each parameter set, one representative strand was analysed, owing to the substantial computational effort associated with reconstruction, machine-learning segmentation, and pore-network quantification. To complement these structurally resolved but non-replicated measurements, porosity was additionally determined using a density-based approach in accordance with Archimedes' principle.

2.5.2. Density-based porosity measurement

The porosity Φ of the extruded foam strands was also determined by density measurements based on Archimedes' principle. For this purpose, the measured foam density ρ_f was related to the bulk density ρ_b of the base polymer according to

$$\Phi = 1 - \frac{\rho_f}{\rho_b}. \tag{5}$$

Measurements were carried out using the ME204T/00 analytical balance from Mettler-Toledo GmbH in combination with the ME-DNY-43 density determination kit. For each strand, five sections of approximately 1.5 cm length were cut at evenly spaced positions along the extrudate. Each section was weighed in air and subsequently in a water bath in accordance with Archimedes' principle. Air bubbles adhering to the surface during immersion were carefully removed using tweezers to avoid measurement errors. Each section was measured three times, and the sample was fully dried between successive measurements to eliminate moisture-induced bias.

2.5.3. Microscopy

Sample Preparation

Polished cross-sections of the extruded polymer strands were prepared for microscopic analysis. Therefore, segments were mounted on a 1 mm thick polymer disc using double-sided adhesive tape and cold-embedded in EpoClear resin supplied by Schmitz-Metallographie GmbH. Grinding was performed semi-automatically using an AutoMet300 Pro manufactured by Buehler Ltd. with identical rotation directions of specimen holder and grinding plate at 60 min^{-1} and 200 min^{-1}, respectively. The grinding sequence started with SiC paper of P600 grit and was gradually refined to P1000, P2500, and P4000, with intermediate inspections. Ultrasonic cleaning in ethanol was performed between steps. Polishing was carried out in two stages using diamond suspensions of 3 μm and 1 μm particle size. Each polishing step was preceded by ultrasonic cleaning and applied under constant load of 10 N, with a final cleaning for 15 min in ethanol. All prepared specimens were subsequently analysed using scanning electron microscopy and optical microscopy.

Scanning electron microscopy

High-resolution images of the cross sections as well as of the strand surfaces were acquired using a LEO Gemini 1530 scanning electron microscope manufactured by Carl Zeiss AG. The specimens were fixed to the sample holder with conductive adhesive tape and electrically contacted using silver paste. A thin gold layer was subsequently deposited in a sputter coater of type 108auto, produced by Cressington Scientific Instruments, with a coating time of 40 s. Imaging was performed at an acceleration voltage of 4.5 kV in secondary electron mode using an in-lens detector.

Optical microscopy

Optical microscopy was carried out using an interference microscope of type Aristoplan, manufactured by Ernst Leitz Wetzlar GmbH. The microscope was connected to a PC via a digital camera unit, enabling direct image acquisition and documentation. No optical filters or contrast-enhancing techniques were applied during imaging.

3. Results

Fig. 6 shows representative longitudinal μCT sections of extruded strands. Bright areas correspond to PLA, while dark regions indicate gas inclusions. The fine-grained, low-contrast dark regions – e.g., in configuration v2–T230–p30 – represent typical μCT image noise rather than actual gas inclusions. The coloured frame indicates extrusion stability: Green indicates unobstructed and continuous extrusion, orange signifies unstable conditions caused by temporary stoppages of the feed gear within the extruder, and red marks severely blocked extrusion, where the feed mechanism jammes to the extent that less than 10 % of the intended feed rate is extruded. At the highest investigated gas pressure of 50 bar, strands could only be analysed for the following configurations: v0.5–T230–p50, v2–T230–p50, v2–T260–p50, and v3.5–T230–p50. Owing to cumulative damage caused by repeated exposure to 50 bar gas pressure, the M2.5 thread used to mount the gas inlet tube in the modular nozzle failed during the study, limiting the number of analyzable configurations at this pressure level.

In cases of unstable or blocked extrusion, the polymer melt remains in the nozzle for an extended period until it is sufficiently heated for its viscosity – and thus the required extrusion pressure – to decrease. During this time, gas continues to flow into the system, which distorts the foam structure within the strand. For this reason, only parameter configurations that allow stable extrusion are considered for analyses. As feed rate increases, fewer parameter configurations remain extrudable under stable conditions (see Fig. 6). Within a given feed rate, increasing temperature and gas pressure improves process stability (see Fig. 6(b) and Fig. 6(c)). For stable configurations, two key trends in foam morphology are observed. First, both the mean pore diameter and total porosity increase with rising gas pressure, independent of T_N and v. For pore density, however, no consistent trend with gas pressure is observed. Second, higher nozzle temperatures promote a more homogeneous distribution of gas inclusions across the strand cross section. These effects are jointly illustrated in Fig. 7, which shows that at low T_N and p_G (see Fig. 7c), gas inclusions are predominantly located near the surface and aligned in linear patterns, whereas at higher temperatures, gas inclusions are uniformly dispersed throughout the cross section (see Fig. 7a). As the gas pressure increases, the gas inclusions become visibly larger with a similarly homogeneous distribution (see Fig. 7b). Fig. 8 further highlights the influence of nozzle temperature on surface morphology by comparing SEM images of configurations v0.5–T260–p30 and v0.5–T200–p30. At the lower temperature (Fig. 8a), a significantly more pronounced formation of surface pores is evident.

These qualitative observations are corroborated by the quantitative results for porosity and mean pore diameter shown in Fig. 9. For the evaluation, only those parameter configurations with stable extrusion behaviour are considered, as process instability, particularly at the highest feed rate of 3.5 mm s^{-1}, prevents meaningful comparison across conditions. The diagrams show that the porosity values obtained by the different methods (CT: μCT and A: Archimedes) vary in magnitude depending on the parameter configuration. For each configuration, the porosity determined via Archimedes' method exceeds the corresponding μCT value. This discrepancy can be explained by methodological differences between the two measurement approaches. From an imaging-related perspective, μCT cannot resolve pores close to or below the Nyquist-limited spatial resolution, which corresponds to approximately 2× the voxel size (≈15.6 µm). SEM analysis of representative strand cross-sections occasionally revealed minimum pore diameters down to 10 µm, which therefore remain undetected in the μCT volume. However, such small pores occurred only sporadically and the majority of pores were larger than the effective resolution limit; hence, resolution alone cannot account for the full deviation. The dominant contribution to the discrepancy arises from the fundamentally different sampling strategies of the two methods. The Archimedes approach integrates the density of five independently measured strand sections and therefore captures heterogeneities along the extrudate. In contrast, μCT quantifies porosity within a single, locally defined volume of interest and – owing to segmentation constraints – only in regions without pronounced surface-connected voids or macropores. As a result, μCT systematically underestimates porosity compared to the globally averaged Archimedes measurements. At v = 0.5 mm s^{-1}, the Archimedes values increase consistently with gas pressure across all examined T_N levels (see Fig. 9(a)). For example, at 200 °C, porosity rises from 21 % at 30 bar to 28 % at 40 bar; at 230 °C, from 26 % to 27 % across the range 30 bar to 50 bar; and at 260 °C, porosity remains approximately constant at 27 %. A similar tendency is observed for the μCT-derived values, although the correlation is less pronounced at 230 °C. A comparable behaviour emerges for the mean pore diameters (Fig. 9(b)), computed as the arithmetic mean of all detected pores. With the exception of configuration v0.5–T230–p40, a pressure-dependent increase is evident. The pore density follows this trend in the opposite direction, decreasing as pores grow larger. At 200 °C, the mean pore diameter increases from 82 µm to 104 µm, while the pore density decreases from 4.8×10^5 cm^{-3} to 4.64×10^5 cm^{-3}. At 260 °C, the pore diameter rises from 100 µm to 126 µm, accompanied by a decrease in pore density from 5.05×10^5 cm^{-3} to 3.03×10^5 cm^{-3}. At 230 °C, the mean diameter decreases from 98 µm to 90 µm at 40 bar, before increasing to 106 µm at 50 bar; the corresponding pore densities rise from 3.77×10^5 cm^{-3} to 5.4×10^5 cm^{-3}, and subsequently drop to 2.84×10^5 cm^{-3}. For v = 2 mm s^{-1}, the stable parameter configurations exhibit analogous trends (see Figs. 9(c) and 9(d)). At 230 °C, porosity increases from 0 % at 40 bar to 16 % (CT) and 21 % (Archimedes) at 50 bar. Consistent with this, no pores are detected at 40 bar, whereas at 50 bar the pore density reaches 4.56×10^4 cm^{-3}. At 260 °C, porosity rises from 9 % to 19 % (CT) and from 9 % to 28 % (Archimedes). The pore diameters follow the same pattern, increasing from 92 µm to 112 µm at 260 °C, and from 0 µm to 93 µm at 230 °C. At 260 °C, the pore density deviates from the previously observed inverse correlation with pore diameter: it initially increases from 2.34×10^5 cm^{-3} to 5.52×10^5 cm^{-3} as pressure rises from 30 bar to 40 bar, despite the concurrent increase in mean pore diameter, before decreasing again to 3.24×10^5 cm^{-3} at 50 bar. Fig. 10 presents the statistical distribution of the porosity values obtained via the Archimedes method for each parameter configuration. Each box plot represents five strand sections, with each section corresponding to the mean of three independent measurements. The mean values shown here therefore directly correspond to those in Fig. 9(a) and Fig. 9(c). The width of the boxes and whiskers varies considerably across the parameter sets, indicating different levels of porosity heterogeneity along the strand. For the feed rate of v = 0.5 mm s^{-1} (see Fig. 10(a)), the whiskers are widest at a nozzle temperature of 230 °C across all pressure levels. The strongest axial inhomogeneity is observed for configuration v0.5–T230–p40, where the interquartile range spans from 16 % to 28 %. The maximum porosity reaches 28.7 %, while the minimum drops to 7.9 %. In contrast, the lowest heterogeneity is found for v0.5–T260–p30 and v0.5–T260–p40, where the interquartile ranges narrow to 26 % to 28 % and 26 % to 27 %, respectively, and the whiskers extend only from 24 % to 29 % and from 25 % to 29 %. Intermediate variability is observed for v0.5–T200–p30 and v0.5–T200–p40. For the higher feed rate of v = 2 mm s^{-1} (see Fig. 10(b)), the mean porosities are lower compared to the corresponding settings at v = 0.5 mm s^{-1} for identical temperature–pressure combinations. The relative widths of the interquartile ranges and whiskers are comparable between the two stable configurations, indicating similar levels of axial variation in porosity.

4. Discussion

4.1. Evaluation of the dominant foaming mechanism under process conditions

According to Henry's law, the equilibrium concentration of a gas dissolved in a polymer melt, c_s, is proportional to the solubility coefficient H and the partial pressure p of the gas [30]:

$$c_s = H \times p \tag{6}$$

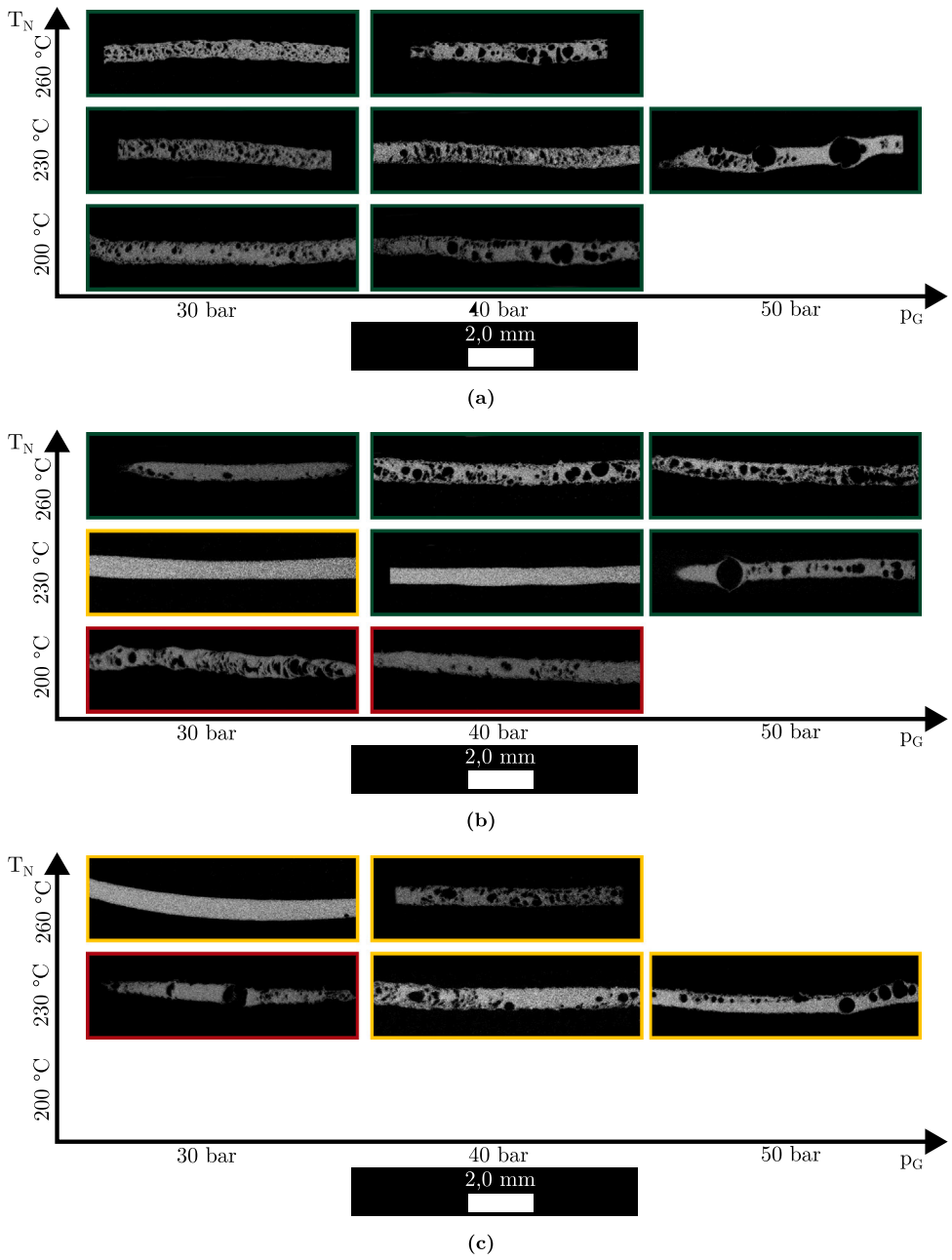

Fig. 6. μCT evaluation of strands extruded at different feed rates. Each image shows a longitudinal cross-section through the centre of the strand segment. The coloured frame indicates extrusion stability: Green for stable extrusion, orange for intermittent extrusion, and red for blocked extrusion. (a) $v = 0.5$ mm/s, (b) $v = 2$ mm/s, (c) $v = 3.5$ mm/s.

Preliminary experiments conducted at a nozzle temperature of 200 °C and a feed rate of 0.5 mm s^{-1} indicated that gas injection into the polymer melt ceased at external gas pressures below approximately 25 bar. This observation, confirmed by the absence of visible gas inclusions in μCT scans, suggests that the melt pressure inside the nozzle counteracts the injection at this threshold, resulting in zero net gas inflow. Based on this, a maximum effective overpressure of approximately 15 bar can be assumed under the highest applied gas pressure of 40 bar. Using literature data for the solubility of CO_2 in PLA at 200 °C [31], the resulting maximum equilibrium gas content can be estimated at around 0.5 wt% under these conditions. In contrast, conventional physical foaming processes based on gas dissolution typically operate at significantly lower temperatures and higher absolute gas pressures, achieving gas contents of up to 20 wt% to 30 wt% in the polymer matrix [31,32]. Moreover, such processes rely on long saturation times to achieve equilibrium solubility and subsequent homogeneous nucleation upon depressurization. In the present configuration, however, the short residence time of the melt inside the nozzle – on the order of a few seconds – renders gas sorption and equilibrium diffusion negligible. As a result, classical physical foaming driven by gas dissolution and supersaturation can be ruled out as the dominant mechanism. Instead, the observed foam structure is primarily attributed to mechanical foaming: gas is introduced directly into the melt through fine orifices in the porous SPM insert, creating microbubbles via local shear and turbulence. This mechanism is widely used for gas dispersion in liquids [33], yet has not been previously applied in the context of FFF. Unlike diffusion-driven foaming, this mechanically induced approach allows for direct control over the local foaming behaviour by adjusting the applied gas

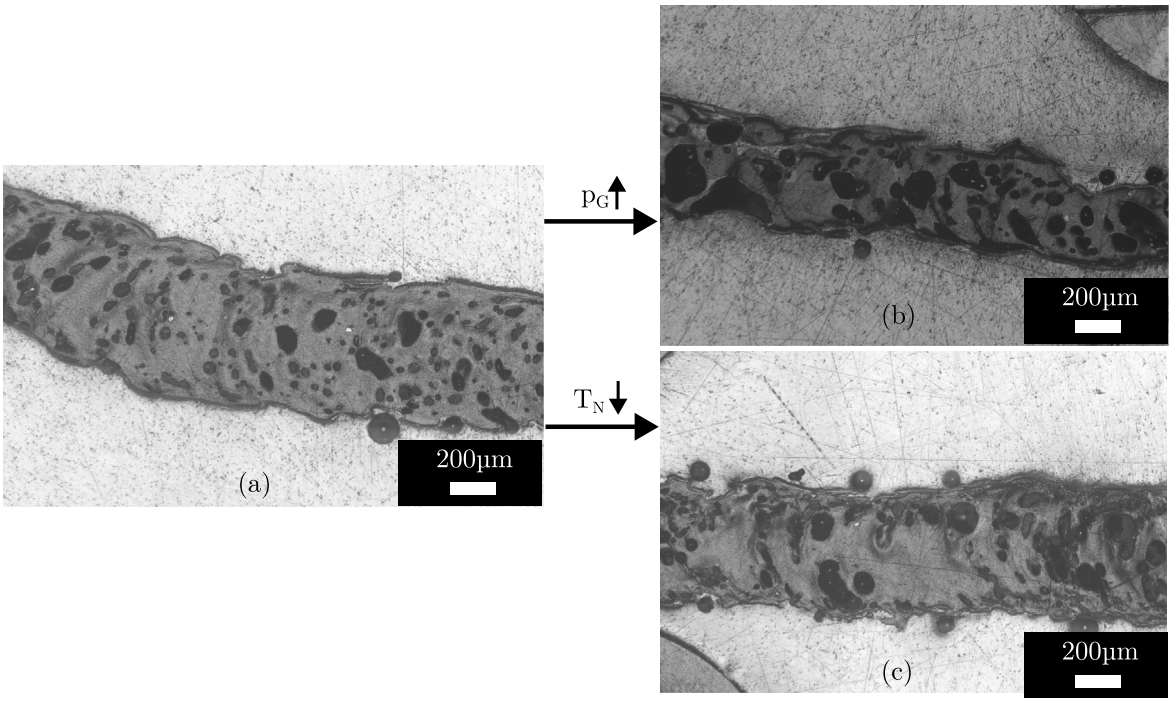

Fig. 7. Effect of temperature and gas pressure on the foam structure. Shown are polished cross-sections of three strands, captured by optical microscopy. Strands produced with configuration (a): v0.5–T260–p30; (b): v0.5–T260–p40, (c): v0.5–T200–p30.

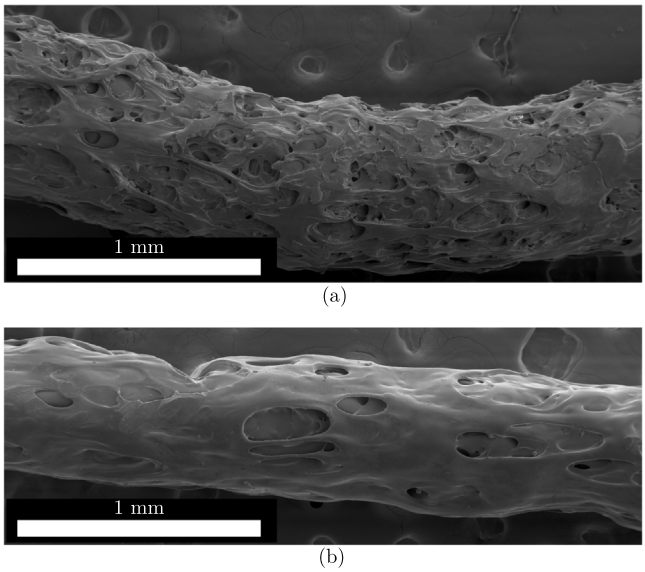

Fig. 8. Effect of nozzle temperature on the strand surface. Shown are SEM images of (a): v0,5-T200-p30 and (b): v0,5-T260-p30.

pressure. This opens up the possibility of dynamically varying the foam density during a build and even producing fully unfoamed layers using the same nozzle.

4.2. Influence of process parameters on extrusion stability

The stability of the extrusion process for a given parameter set primarily depends on whether the pressure generated by the extrusion mechanism is sufficient to overcome the pressure drop within the nozzle. This pressure drop can be approximated using the Hagen–Poiseuille equation under the assumptions of steady, laminar flow of an incompressible, Newtonian fluid through a channel of constant and idealized cylindrical geometry [34,35]:

$$Q = \frac{\Delta p \cdot \pi \cdot d^4}{128 \cdot \eta \cdot l}, \tag{7}$$

where Δp is the pressure difference, d and l are the diameter and length of the channel, respectively, and η is the dynamic viscosity of the fluid. The volumetric flow rate Q can also be expressed as a function of the feed rate v and the filament cross-sectional area A, under the assumption of negligible slip between the drive system and the filament as well as constant filament geometry:

$$Q = v \cdot A \quad \text{with} \quad A = \frac{\pi d_F^2}{4}, \tag{8}$$

where d_F is the diameter of the incoming filament. Substituting Eq. (8) into Eq. (7) yields:

$$\Delta p = \frac{32 \cdot L \cdot \eta \cdot v \cdot d_F^2}{d_D^4}, \tag{9}$$

where d_D is the diameter of the nozzle and L its effective length. This relation reveals that, for a fixed nozzle geometry, the pressure loss is primarily governed by the viscosity η of the polymer melt and the feed rate v. Since the viscosity increases exponentially with decreasing temperature in accordance with the Arrhenius equation [36], the pressure drop that must be overcome by the extruder increases at lower nozzle temperatures. Such a temperature decrease may be caused either by a lower set temperature or by reduced heat transfer owing to an increased feed rate. Thus, feed rate affects the pressure drop in two ways: directly, by increasing the flow velocity, and indirectly, by limiting thermal input and thereby increasing viscosity. These relationships explain the extrusion behaviour observed in Fig. 6: At the lowest investigated feed rate of $0.5\,\mathrm{mm\,s^{-1}}$, extrusion is stable across all combinations of nozzle temperature and gas pressure. Increasing the feed rate to $2\,\mathrm{mm\,s^{-1}}$ leads to complete blockage at the lowest temperature level of 200 °C, as the pressure drop across the nozzle, caused by the markedly increased melt viscosity at low temperature and higher flow velocity, exceeds the maximum pressure that can be

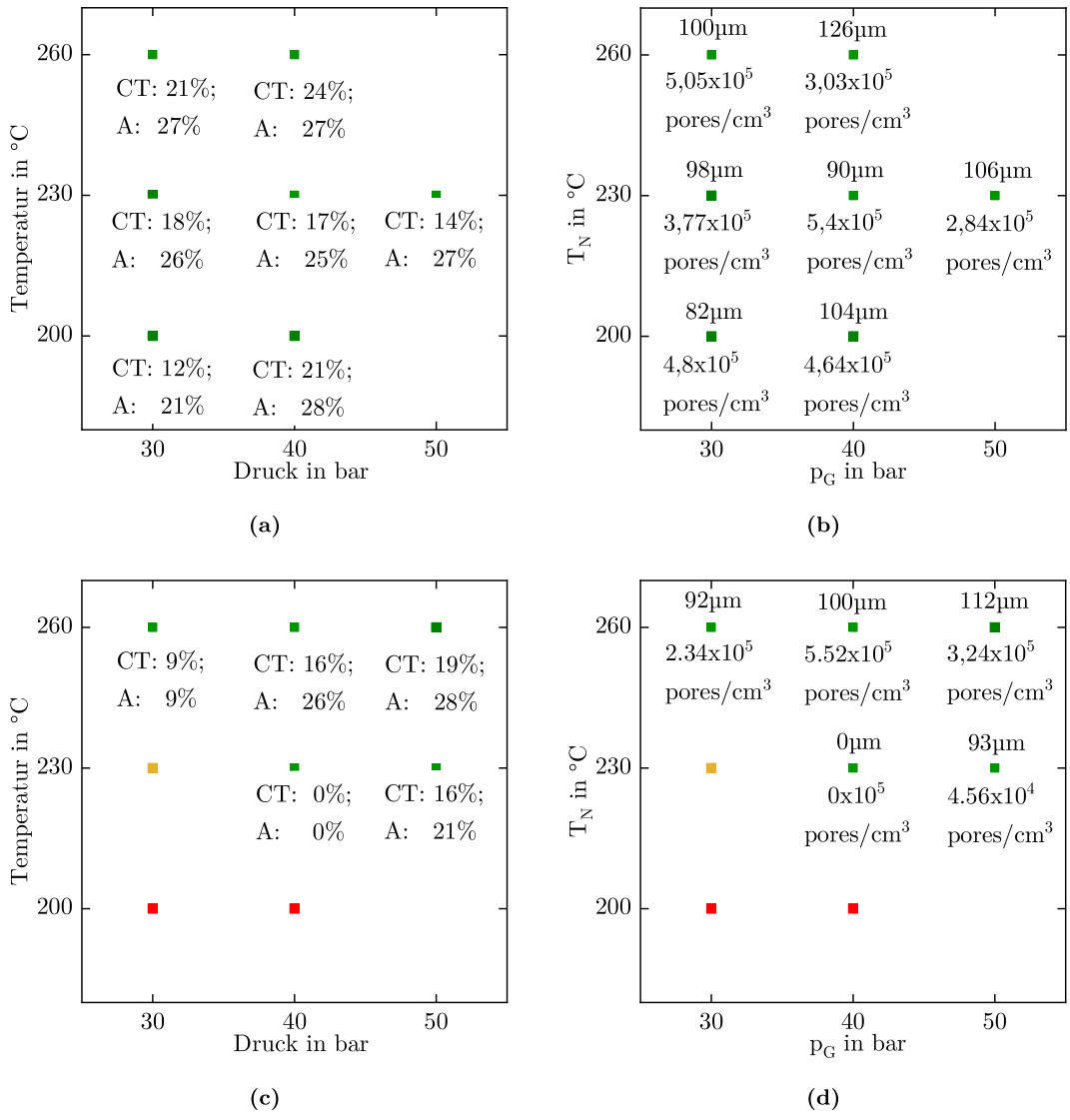

Fig. 9. Mean Porosity ((a) and (c)) and mean pore diameter with pore number density ((b) and (d)) as a function of gas pressure and nozzle temperature for feed rates of $v = 0.5$ mm/s ((a), (b)) and $v = 2$ mm/s ((c), (d)). The coloured frame indicates extrusion stability: green for stable extrusion, orange for intermittent extrusion, and red for blocked extrusion. Only stable configurations are evaluated.

generated by the extrusion mechanism. Raising the temperature to 230 °C enables at least intermittent extrusion, while stable operation is only achieved at 260 °C, where the reduced viscosity lowers the pressure drop. A further increase in feed rate to $3.5\,\mathrm{mm\,s^{-1}}$ results in unstable or blocked extrusion for all tested parameter combinations. Notably, for feed rates of $2\,\mathrm{mm\,s^{-1}}$ and $3.5\,\mathrm{mm\,s^{-1}}$, an increase in gas pressure at 230 °C appears to improve extrusion stability. This effect can be attributed to the higher amount of dissolved CO_2 at elevated pressures, which acts as a physical plasticizer and reduces the melt viscosity of PLA [37–39]. Despite stable extrusion, Fig. 10 shows that the porosity along the strand exhibits different degrees of homogeneity across the individual parameter configurations. It should therefore be noted that a distinction must be made between stable extrusion and stationary foam extrusion. The influence of the process parameters on the resulting foam morphology is therefore examined in the following chapter.

Influence of process parameters on mass flows

At a constant feed rate, the polymer melt flow rate remains, disregarding the variable slip on the drive wheel, constant according to Eq. (8). Multiplying this volumetric flow rate by the density of PLA yields the mass flow rate of the melt $\dot{m}_\mathrm{M}$:

$$\dot{m}_M = \rho_\mathrm{PLA} \cdot Q. \tag{10}$$

At a fixed nozzle temperature, the pressure drop across the nozzle remains approximately constant, resulting in a nearly constant melt pressure within the gas injection zone. To introduce gas into the nozzle, the externally applied gas pressure must exceed this internal melt pressure. Based on the permeability of the PM and the pressure difference between the external gas supply and the melt, a gas mass flow rate ($\dot{m}_G$) into the nozzle is established in accordance with Darcy's law (see Eq. (4)). This gas flow increases with rising pressure difference. To describe the ratio of gas to polymer melt flow quantitatively, the dimensionless mass flow ratio (MR) is introduced:

$$MR = \frac{\dot{m}_\mathrm{G}}{\dot{m}_\mathrm{M}}, \tag{11}$$

where $\dot{m}_\mathrm{G}$ is the gas mass flow rate and $\dot{m}_\mathrm{M}$ is the polymer melt mass flow rate. Increasing the gas pressure at constant feed rate and nozzle temperature consequently leads to a higher MR, meaning more gas is introduced per unit of melt. This explains the experimental observations in Fig. 9, where rising gas pressure correlates with higher foam porosity and larger average gas inclusion diameter. Although its

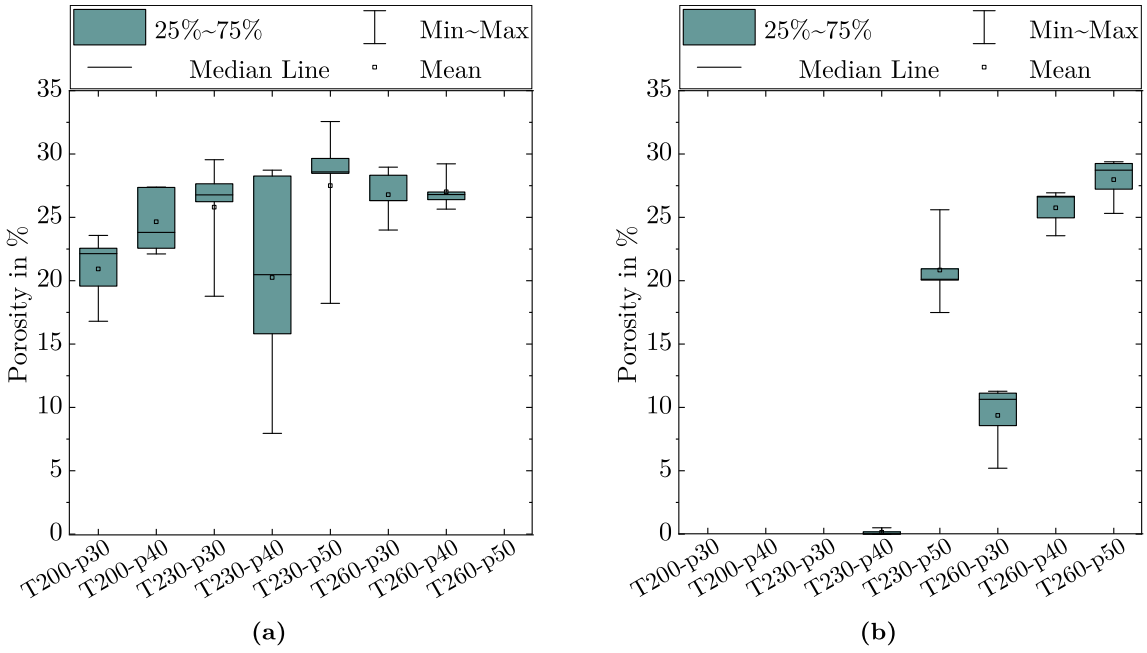

Fig. 10. Porosity distribution along the strand for each parameter set. Each box represents five strand sections (n = 5), where each section is the mean of three independent Archimedes measurements. (a): At $v = 0,5$ mm/s; (b): At $v = 2$ mm/s. Only stable configurations are evaluated.

exact value cannot be determined with the measurement capabilities available in this feasibility study, an optimal mass flow ratio MR_{opt} can be assumed that yields a foam structure characterised by high porosity and a homogeneous distribution of small gas inclusions (high pore density). This structure is referred to here as a *homogeneous fine-cell structure*, and the corresponding qualitative relationships serve as the basis for the subsequent discussion. At a feed rate of $0.5\,\mathrm{mm\,s^{-1}}$, the configuration v0.5–T260–p30 most closely resembles this process-optimized target structure (see Fig. 6(a)). It yields a relatively small mean pore diameter of approximately 100 µm, with porosity values of 21 % to 24 % and a pore density of $5.05 \times 10^5\,\mathrm{cm^{-3}}$, which, according to Eq. (1), correspond to an expansion ratio of up to 32 % (see Fig. 9). This is further supported by cross sections of strands showing a homogeneous internal distribution of gas inclusions (see Fig. 7), and is also reflected in the low porosity scatter along the strand in Fig. 10. The resulting foam quality is comparable to expansion ratios typically achieved using ex-situ foaming approaches with high-pressure autoclaves [6,7]. Increasing the feed rate by a factor of four to $2\,\mathrm{mm\,s^{-1}}$ proportionally increases the melt mass flow rate $\dot{m}_M$ according to Eq. (10). To maintain a comparable foam structure, the gas mass flow rate $\dot{m}_G$ would also need to be increased by the same factor to maintain a similar *MR*. However, in configuration v2–T260–p30, the gas pressure and temperature remain unchanged, resulting in an insufficient increase in $\dot{m}_G$. Consequently, the injected gas volume is too low relative to the melt throughput. Although the average diameter of the gas inclusions remains comparable (92 µm), the porosity drops significantly to 9 % to 12 % and the pore density is less than half, clearly reflecting that $MR < MR_{opt}$. The foam structure presented here is therefore referred to as *inhomogeneous fine-cell structure*. Increasing the gas pressure raises $\dot{m}_G$ and thus shifts MR closer to MR_{opt}, resulting in a more favourable foam structure. For example, at 40 bar, porosity reaches up to 28 %, with the same mean diameter of the gas inclusions and a pore density comparable to that of the process-optimized configuration. The porosity scatter along the strand axis likewise remains low, further indicating a process regime that promotes homogeneous fine-celled structures. This indicates that different parameter combinations can lead to comparable foam morphologies, provided they produce a similar *MR*. This relationship is illustrated qualitatively by the heatmap in Fig. 11. However, technical limitations must be considered: The feed rate cannot be increased arbitrarily owing to the limited extrusion pressure capacity of the extrusion system. Likewise, raising the gas pressure to increase $\dot{m}_G$ is constrained by the mechanical strength of the gas adapter interface, particularly the threaded connection used to mount the gas inlet. Nozzle temperature also has practical limits: too low, and melt viscosity hinders extrusion; too high, and thermal degradation of the polymer may occur. If the mass flow ratio exceeds the optimal value ($MR > MR_{opt}$), gas cannot be evenly dispersed in the melt. Instead, gas inclusions coalesce into larger voids, leading to macrovoid formation; an *inhomogeneous coarse-cell structure* develops. This behaviour is observed for configuration v0.5–T260–p40, where gas pressure is elevated relative to the homogeneous fine-celled case (see Fig. 7). This manifests as an increase in the mean pore size and a decrease in pore density at essentially unchanged porosity (see Fig-. 9.) The phenomenon is particularly pronounced in strands produced with configurations v0.5–T230–p50 and v2–T230–p50 (see Figs. 6(a) and 6(b)). The elevated gas pressure leads to excessive gas flow, especially relative to the low melt flow rate at $0.5\,\mathrm{mm\,s^{-1}}$, which results in large, spherical macrovoids clearly visible in the strand cross sections.

Based on the observed relationships, Fig. 11 presents a derived qualitative process characteristic for a feed rate of $v = 0.5\,\mathrm{mm\,s^{-1}}$, summarising the described interdependencies. With increasing nozzle temperature (ordinate), the melt viscosity η and thus the melt pressure p_M decrease. As a result, the gas mass flow rate $\dot{m}_G$ rises, leading to a higher MR. Increasing gas pressure p_G (abscissa) directly enhances the amount of gas entering the melt and thus the gas mass flow. This effect is further amplified by the additional viscosity reduction caused by the higher amount of dissolved gas, which lowers the nozzle pressure and increases the driving pressure gradient, thereby further increasing the gas inflow and MR. The grey area indicates the feasible process window in which the technical boundary conditions allow for stable and damage-free extrusion. The characteristic behaviour shown within the black box shifts along the arrows when the feed rate is increased, while the process window itself remains unchanged. This illustrates that, although a wide range of parameter combinations may theoretically produce homogeneously microporous foams, the parameter space is practically limited by technical constraints.

Based on the measured pore diameters and -densities, even the homogeneous fine-cell structured foam here falls within the range of

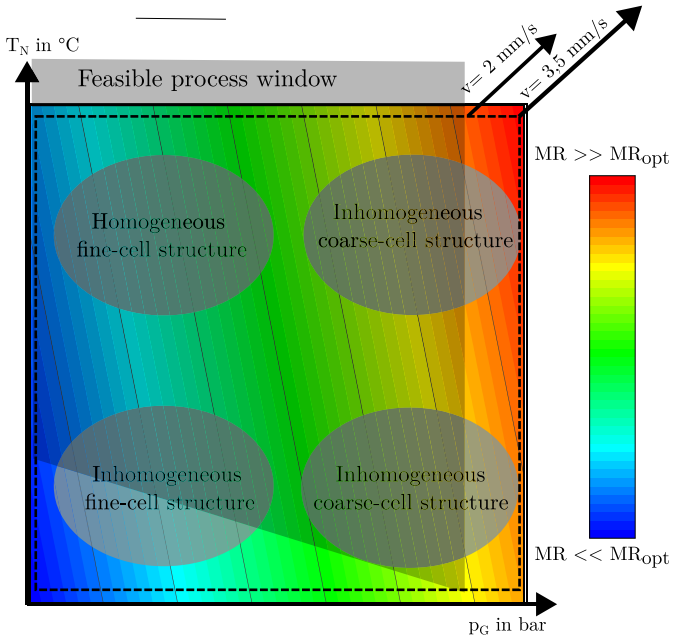

Fig. 11. Summary of key process parameter influences on foaming behaviour: The Heatmap represents the effect of process parameters on the mass flow ratio MR. Shown is the resulting qualitative process characteristic for $v = 0.5\,\mathrm{mm\,s^{-1}}$. The grey box indicates the feasible process window for stable and damage-free extrusion. Increasing the feed rate shifts the characteristic behaviour along the indicated arrows, while the process window itself remains unchanged.

conventional polymeric foams. Microcellular foams (1 µm to 10 µm and pore densities of $10^9\,\mathrm{cm^{-3}}$ to $10^{12}\,\mathrm{cm^{-3}}$) and nanocellular foams (< 1 µm and pore densities higher than $10^{12}\,\mathrm{cm^{-3}}$) exhibit significantly smaller cell diameters and are therefore located well below the structures achieved in the present feasibility study [40]. Future work aiming at a quantitative tuning of the process parameters, grounded in the qualitative mass-flow-ratio relationships established here, will therefore be essential to approach these finer foam classes. Importantly, such optimisation will require dedicated, measurement-supported experiments, including direct acquisition of melt temperature, viscosity, nozzle pressure and gas throughput, which were beyond the scope of this feasibility study. In this context, integrating static mixing elements or other in-nozzle dispersive structures appears particularly promising, as they are expected to enhance gas distribution and promote the formation of smaller, more uniformly dispersed cells [33] — morphologies that are typically associated with improved mechanical and thermal performance [40].

4.3. Integration into commercial FFF systems — practical considerations

The presented foaming approach can be implemented in commercial FFF systems as long as the PM nozzle can be mounted in place of the standard nozzle. If the same Revo-based setup as used in this study is employed, the PM nozzle can be installed directly without further modification. However, if a different nozzle and hot-end configuration is used, the respective nozzle would need to be machined to provide an M6 external thread so that it can serve as a carrier for the modular SPM nozzle (see Chap. 2.3). For safe operation in commercial environments, the gas inlet and all associated sealing interfaces would need to be designed and validated for the maximum operating pressure of the system. This includes appropriate mechanical dimensioning as well as pressure-integrity verification, for example through burst-pressure testing, to ensure a sufficient safety margin against failure. These qualification steps were not part of this feasibility-prototype study and will be required prior to any commercial implementation.

Since the foaming mechanism is predominantly mechanical rather than based on gas dissolution, the use of compressed air instead of CO_2 is a realistic alternative. This would eliminate the need for pressurised CO_2 cylinders and allow integration with standard compressor-based air supplies. Future work should therefore investigate the foaming behaviour obtained with compressed air and compare it to the CO_2-based process. For the fabrication of complete components rather than free extruded strands, a synchronised control of gas pressure and extrusion rate will likely be required. Such a system must dynamically adjust the gas pressure in response to changes in filament feed rate (e.g., during non-print moves, acceleration/deceleration, or direction reversals). Under these conditions, the process could enable the fabrication of parts with locally varying foam densities and sharp transitions between foamed and unfoamed regions — a capability facilitated by the predominantly mechanical nature of the foaming mechanism, which does not rely on diffusion- or solubility-controlled nucleation kinetics.

5. Conclusion

The present work demonstrates that in situ mechanical foaming via direct gas injection into the polymer melt during extrusion is technically feasible. A porous metallic material with submicron pore size within an adapted nozzle effectively enabled gas permeation while preventing polymer melt leakage, proving essential for stable operation. The results highlight that the foam morphology is governed primarily by the mass flow ratio between gas and polymer. At an operating point of the adapted nozzle, which was assumed to provide an optimal ratio of gas to melt mass flow, uniform microporosity was achieved with average pore diameters of approximately 100 µm and porosities around 25 %. Deviations from this condition cause structural inhomogeneities or process instabilities. This mass flow ratio is influenced by the complex interplay of nozzle temperature, feed rate, and gas pressure. While various optimal ratios can theoretically be achieved by adjusting these parameters, the practically realizable process window is constrained. Specifically, the pressure drop across the nozzle, resulting from melt viscosity and flow conditions, must remain below the maximum pressure that can be applied by the extrusion unit.

Compared to established in situ or ex situ foaming strategies in material extrusion, the maximum expansion ratio of 33 % observed in this study remains comparatively low. It should be noted, however, that literature values typically refer to entire printed parts, where additional porosity arises from inter-filament voids. To achieve higher porosity within the strand itself, future work should focus on a more detailed quantification of the gas-to-melt mass flow ratio and a deeper understanding of gas–melt interactions at the interface of the porous material.

Despite these constraints, the developed approach for situ foaming offers significant advantages over conventional extrusion-based methods. It eliminates the need for prior compounding or post-processing in autoclaves, avoids time-dependent gas loss in pre-saturated filaments, and enables direct mechanical injection of gas into the melt. As a result, the porosity becomes a function of controllable process parameters, allowing reproducible foam formation, layer-specific foam/non-foam transitions, and minimal strand expansion. Furthermore, the nozzle can be integrated into existing material extrusion systems with manageable adaptation effort. Given that mechanical foaming has not yet been utilized in additive manufacturing despite its broad industrial relevance, the presented approach offers substantial potential for further development.

CRediT authorship contribution statement

Lars Eisele: Writing – original draft, Visualisation, Validation, Methodology, Investigation, Formal analysis. **Anselm Heuer:** Writing – review & editing, Project administration, Methodology, Formal analysis, Conceptualisation. **Wilfried V. Liebig:** Writing – review & editing, Supervision, Resources, Funding acquisition, Conceptualisation.

Declaration of Generative AI and AI-assisted technologies in the writing process

During the preparation of this work, the authors used DeepL and DeepL Write (DeepL SE, Germany) to improve the readability and language of the manuscript. Having used these tools, the authors reviewed and edited the content as necessary, taking full responsibility for the publication's content.

Declaration of competing interest

The authors declare that they have no known competing financial interests or personal relationships that could have appeared to influence the work reported in this paper.

Acknowledgements

This research was funded by the Deutsche Forschungsgemeinschaft (DFG, German Research Foundation), Germany, grant number EL 473/10-1 and LI 3675/4-1. Finally, we acknowledge support by the KIT-Publication Fund of the Karlsruhe Institute of Technology.

Data availability

Data will be made available on request.

References

[1] M. Nofar, J. Utz, N. Geis, V. Altstädt, H. Ruckdäschel, Foam 3D printing of thermoplastics: A symbiosis of additive manufacturing and foaming technology, Adv. Sci. 9 (11) (2022) 2105701.
[2] D. Eaves, Handbook of Polymer Foams, iSmithers Rapra Publishing, 2004.
[3] S.-T. Lee, C.B. Park, Foam Extrusion: Principles and Practice, CRC Press, 2014.
[4] G. Wypych, Handbook of Foaming and Blowing Agents, Elsevier, 2022.
[5] A.L. Heuer, Prozess- Und Werkstoffcharakterisierung Von Im ARBURG Kunststoff-Freiform-Verfahren Hergestellten, in Situ Geschäumten Strukturen (Ph.D. thesis), Karlsruher Institut für Technologie (KIT), 2024.
[6] B.K. Park, D.J. Hwang, D.E. Kwon, T.J. Yoon, Y.-W. Lee, Fabrication and characterization of multiscale PLA structures using integrated rapid prototyping and gas foaming technologies, Nanomaterials 8 (8) (2018) 575.
[7] B. Sun, L. Wu, Research progress of 3D printing combined with thermoplastic foaming, Front. Mater. 9 (2022-11-28) Publisher: Frontiers.
[8] M. Li, J. Jiang, B. Hu, W. Zhai, Fused deposition modeling of hierarchical porous polyetherimide assisted by an in-situ CO2 foaming technology, Compos. Sci. Technol. 200 (2020) 108454.
[9] J. Zhang, D. Li, W. Zhu, Y. Li, In situ 3D printing of poly-ether-ether-ketone/poly-ether-imide hierarchical cellular foams containing electromagnetic absorbent, Addit. Manuf. 59 (2022) 103181.
[10] M.G.M. Marascio, J. Antons, D.P. Pioletti, P.-E. Bourban, 3D printing of polymers with hierarchical continuous porosity, Adv. Mater. Technol. 2 (11) (2017) 1700145.
[11] A. Damanpack, A. Sousa, M. Bodaghi, Porous PLAs with controllable density by FDM 3D printing and chemical foaming agent, Micromachines 12 (8) (2021) 866.
[12] K. Zarybnicka, P. Lepcio, J. Svatik, J. Jancar, F. Ondreas, Effect of the nanoparticles on the morphology and mechanical performance of thermally blown 3D printed HIPS foams, J. Appl. Polym. Sci. 140 (5) (2023) e53413.
[13] K. Kalia, B. Francoeur, A. Amirkhizi, A. Ameli, In situ foam 3D printing of microcellular structures using material extrusion additive manufacturing, ACS Appl. Mater. Interfaces 14 (19) (2022-05-18) 22454–22465.
[14] K. Kalia, A. Ameli, Additive manufacturing of functionally graded foams: Material extrusion process design, part design, and mechanical testing, Addit. Manuf. 79 (2024) 103945.
[15] A. Pawar, G. Ausias, Y.-M. Corre, Y. Grohens, J. Férec, Mastering the density of 3D printed thermoplastic elastomer foam structures with controlled temperature, Addit. Manuf. 58 (2022) 103066.
[16] K. Kalia, A. Ameli, Understanding the process-microstructure-property relationships in material extrusion additive manufacturing of polylactic acid microcellular foams, Addit. Manuf. 72 (2023) 103636.
[17] Z. Zhou, K. Ruan, D. Zhao, X. Xu, Z. Chen, Y. Xiong, Spatiotemporal monitoring and control for foam additive manufacturing processes of thermoplastics, Addit. Manuf. (2025) 104949.
[18] C. Esposito, D. Tammaro, P. Posabella, M.M. Villone, G. D'Avino, P.L. Maffettone, Orientation-graded morphologies in microcellular foams through additive manufacturing, Ind. Eng. Chem. Res. 63 (42) (2024) 17949–17960.
[19] D. Tammaro, R. Della Gatta, M.M. Villone, P.L. Maffettone, Continuous 3D printing of hierarchically structured microfoamed objects, Adv. Eng. Mater. 24 (5) (2022) 2101226.
[20] E.M. Agaliotis, B.D. Ake-Concha, A. May-Pat, J.P. Morales-Arias, C. Bernal, A. Valadez-Gonzalez, P.J. Herrera-Franco, G. Proust, J.F. Koh-Dzul, J.G. Carrillo, E.A. Flores-Johnson, Tensile Behavior of 3D Printed Polylactic Acid (PLA) Based Composites Reinforced with Natural Fiber, Polymers 14 (19) (2022) 3976, Number: 19 Publisher: Multidisciplinary Digital Publishing Institute.
[21] B. Freeland, E. McCarthy, R. Balakrishnan, S. Fahy, A. Boland, K.D. Rochfort, M. Dabros, R. Marti, S.M. Kelleher, J. Gaughran, A Review of Polylactic Acid as a Replacement Material for Single-Use Laboratory Components, Materials 15 (9) (2022) 2989, Number: 9 Publisher: Multidisciplinary Digital Publishing Institute.
[22] J. Orellana Barrasa, A. Ferrández-Montero, B. Ferrari, J.Y. Pastor, Characterisation and Modelling of PLA Filaments and Evolution with Time, Polymers 13 (17) (2021) 2899.
[23] Y. Wu, X. Gao, J. Wu, T. Zhou, T.T. Nguyen, Y. Wang, Biodegradable Polylactic Acid and Its Composites: Characteristics, Processing, and Sustainable Applications in Sports, Polymers 15 (14) (2023) 3096, Number: 14 Publisher: Multidisciplinary Digital Publishing Institute.
[24] Ineos Styrolution Group GmbH, CAMPUS Datenblatt Terluran GP-35 - ABS, 2018, INEOS Styrolution Europe GmbH. Chemie Wirtschaftsförderungsgesellschaft (CWFG) GmbH, Frankfurt am Main, Deutschland..
[25] J. Bear, Modeling Phenomena of Flow and Transport in Porous Media, in: Theory and Applications of Transport in Porous Media, vol. 31, Springer International Publishing, Cham, 2018.
[26] J. Bear, Dynamics of Fluids in Porous Media, Courier Corporation, 2013.
[27] K. Koller, C. Paulik, C. Burgstaller, Influence of material contamination on polypropylene melt filtration using assembled and fused screens, SPE Polym. 3 (1) (2022) 12–24.
[28] F. Carrasco, O. Santana Perez, M.L. Maspoch, Kinetics of the thermal degradation of poly (lactic acid) and polyamide bioblends, Polymers 13 (22) (2021) 3996.
[29] M. Hutchinson, A. O'Donohue, B. Eslami, K. Fouladi, Numerical and experimental analysis of 3D printer hot ends, Discov. Appl. Sci. 6 (5) (2024) 213.
[30] D.W. Van Krevelen, K. Te Nijenhuis, Properties of Polymers: Their Correlation with Chemical Structure; Their Numerical Estimation and Prediction from Additive Group Contributions, Elsevier, 2009.
[31] G. Li, H. Li, L. Turng, S. Gong, C. Zhang, Measurement of gas solubility and diffusivity in polylactide, Fluid Phase Equilib. 246 (1–2) (2006) 158–166.
[32] E. Aionicesei, M. Škerget, Ž. Knez, Measurement of CO2 solubility and diffusivity in poly (l-lactide) and poly (d, l-lactide-co-glycolide) by magnetic suspension balance, J. Supercrit. Fluids 47 (2) (2008) 296–301.
[33] W. Drenckhan, A. Saint-Jalmes, The science of foaming, Adv. Colloid Interface Sci. 222 (2015) 228–259, Reinhard Miller, Honorary Issue.
[34] Y. Nakayama, Introduction to Fluid Mechanics, Butterworth-Heinemann, 2018.
[35] M.C. Potter, B.H. Ramadan, An Introduction to Fluid Mechanics, Springer, 2025.
[36] A. Bellini, S. Guceri, M. Bertoldi, Liquefier Dynamics in Fused Deposition, J. Manuf. Sci. Eng. 126 (2) (2004) 237–246.
[37] D. Dörr, T. Standau, S. Murillo Castellón, C. Bonten, V. Altstädt, Rheology in the presence of carbon dioxide (CO2) to study the melt behavior of chemically modified polylactide (PLA), Polymers 12 (5) (2020) 1108.
[38] T. Schaible, C. Bonten, In-line measurement and modeling of temperature, pressure, and blowing agent dependent viscosity of polymer melts, Appl. Rheol. 32 (1) (2022) 69–82.
[39] D. Raps, H.G. Hosseinabadi, L. Heymann, T. Köppl, V. Altstädt, Rheological properties of thermoplastic polymers with dissolved gases for foaming applications, 2018, arXiv preprint arXiv:1804.07956.
[40] T. Azdast, R. Hasanzadeh, Increasing cell density/decreasing cell size to produce microcellular and nanocellular thermoplastic foams: A review, J. Cell. Plast. 57 (5) (2021) 769–797, http://dx.doi.org/10.1177/0021955X20959301.